Journal of Materiomics 11 (2025) 100892

Contents lists available at ScienceDirect

Journal of Materiomics

journal homepage: www.journals.elsevier.com/journal-of-materiomics/

Research paper

High performance composite phosphor-in-glass film for laser-driven warm white light on patterned sapphire substrate

Wenting Ding [a], Shuai Yang [a], Xin Hou [a], Tao Yang [a], Rongbin Xu [a, **], Yang Mei [a], Leiying Ying [a], Miao Lu [b], Baoping Zhang [a, c, d, *]

[a] Department of Microelectronics and Integrated Circuits, Laboratory of Micro/Nano-Optoelectronics, School of Electronic Science and Engineering, Xiamen University, Xiamen, 361005, Fujian, China
[b] Pen-Tung Sah Research Institute of Micro-Nano Science & Technology, Xiamen University, Xiamen, 361005, Fujian, China
[c] Institute of Nanoscience and Applications, Southern University of Science and Technology, Shenzhen, 518055, Guangdong, China
[d] School of Optoelectronic Information, Minnan Science and Technology University, Quanzhou, 362332, Fujian, China

ARTICLE INFO

Article history:
Received 27 December 2023
Received in revised form
29 March 2024
Accepted 13 April 2024
Available online 30 July 2024

Keywords:
Patterned sapphire substrate
Phosphor-in-glass film
High performance
Laser lighting

ABSTRACT

Phosphor-in-glass film (PiF) based on sapphire substrate (SS) is a promising laser-driven color converter. Herein, by using an optimized silicon borate glass component, high-performance $Y_3Al_5O_{12}:Ce^{3+}$ PiFs are successfully prepared on both flat sapphire substrate (FSS) and patterned sapphire substrate (PSS) surfaces. Compared with planar structure of FSS, PSS has a periodic arrangement of conical structures on its surface, which effectively increases the contact area between the PiF and the substrate by approximately 56%, thereby forming a more robust film composite structure. The blue laser light is affected by the structure of PSS and produces a typical diffraction effect, which realizes the dispersion of the convergent beam. This significantly expands the laser spot on PSS-PiF and improves the uniformity of light. The saturation power density of PiF-PSS (6.29 W/mm^2) is found to be 91% higher than that of PiF-FSS, while maintaining a high luminous efficiency (220 lm/W) and a low correlated color temperature (4500 K). Finally, the thermal quenching mechanism of PiF with different substrate surface morphologies is compared and analyzed. The present results provide important support for designing the interface structure between SSs and PiF to achieve higher efficiency and higher saturation threshold for warm white light.

1. Introduction

With the beginning of the new century, the high-tech industry has experienced explosive development around the semiconductor industry. Among them, solid-state lighting technology based on gallium nitride-based light emitting diode (LED) chips has attracted widespread attention in the lighting industry by exciting efficient and stable phosphor conversion materials to achieve high-performance light sources [1–3]. In various fields such as automotive headlights, engineering lighting, aviation and aerospace lighting, and marine lighting, the demand for high-power solid-state lighting is increasing [4]. Due to the well-known issue/problem of "decreasing efficiency" in LED lighting technology, the laser diode (LD) based lighting technology, which has the advantages of low cost, high luminous flux (LF), and ultra-high output power, has received more attention. In present laser lighting technology, however, makes the combination of phosphor powder + silica gel or organic resin is difficult to maintain stable operation under high-intensity laser irradiation [5–7]. Therefore, inorganic phosphor conversion materials with excellent thermal conductivity and thermal resistance, such as phosphor glass, phosphor ceramics, and phosphor single crystals, are the best partners for laser lighting [8,9]. Among the above phosphor materials, phosphor ceramics and phosphor single crystals have excellent performance, but their preparation processes are complex, their production costs are too high, and they are not suitable for industrial production needs [10–12]. In contrast, phosphor glass, with its simple preparation process and low production cost, can promote the development

* Corresponding author. Department of Microelectronics and Integrated Circuits, Laboratory of Micro/Nano-Optoelectronics, School of Electronic Science and Engineering, Xiamen University, Xiamen, 361005, Fujian, China.
** Corresponding author.
E-mail addresses: xurongbin@xmu.edu.cn (R. Xu), bzhang@xmu.edu.cn (B. Zhang).
Peer review under responsibility of The Chinese Ceramic Society.

https://doi.org/10.1016/j.jmat.2024.04.014

and popularization of the laser lighting industry while ensuring competitive luminescent performance [13].

Currently, research on phosphor glass materials includes the following methods: spontaneous precipitation of phosphor crystals in a glass matrix, rapid cooling of a mixture of phosphor and glass powders, sintering of phosphor and glass powders, and sintering of a mixture of phosphor and glass powders coated on substrates such as sapphire single crystals, quartz glass, ceramics, and metals [14,15]. Due to the amorphous structure of glass, its thermal conductivity is often lower than that of polycrystalline or single crystal materials, which is an important limitation in the improvement of phosphor glass performance. Therefore, the phosphor-in-glass film (PiF) based on high thermal conductivity substrates has outstanding performance and sustainability [16]. On the other hand, $Y_3Al_5O_{12}:Ce^{3+}$ (YAG:Ce) structure-based garnet-type phosphor is widely recognized because of its typical broad yellow emission band, high quantum efficiency, high physicochemical stability, and low production cost, and is often used as the main luminescent center and co-sintered with glass to prepare PiFs [17,18]. Xiang *et al.* achieved a high luminous efficiency (LE) of up to 250 lm/W by co-firing YAG:Ce and quartz glass on the surface of a flat sapphire substrate (FSS) to obtain PiF [19]. Xie *et al.* redesigned the FSS-based PiF structure to withstand laser irradiation up to 11.2 W/mm^2, resulting in an output LF of up to 1839 lm [20]. Meanwhile, Chen *et al.* sintered YAG:Ce and $CaAlSiN_3:Eu^{2+}$ phosphors on an aluminum plate, reducing the operating temperature of PiF to below 35 °C under laser irradiation of 5.6 W power [12]. Clearly, FSS has the advantages of high thermal conductivity (~30 W/(m·K)) and visible light transmittance (~85%) and low cost, making it suitable as a carrier for PiF and easier to achieve high LF and LE [21]. However, there are still some issues with FSS-based PiF, such as the ineffective adhesion between glass and FSS, which leads to PiF fragmentation or detachment, as well as serious laser reflection problems caused by the interface effect between the membrane layer and FSS. Unlike FSS, patterned sapphire substrate (PSS), where a three-dimensional patterned microstructure is created on the surface of a sapphire substrate (SS) through semiconductor etching technology, is mainly used to solve the lattice mismatch of gallium nitride materials to improve the quality of crystal growth and can also serve as diffractive optical elements to increase light scattering and enhance light extraction efficiency [22–25]. It is worth noting that there has been no report on both the preparation and the laser lighting performance of PiF on the microstructure surface of PSS.

Here, we have redesigned the matrix glass of silicate components and used low-temperature co-sintering to solidify YAG:Ce phosphor powders and glass powders, on the surfaces of FSS and PSS, respectively, to obtain PiF. According to the results of structure and luminescence properties, YAG:Ce PiF maintains the excellent luminescence characteristics of the original phosphor powder. In the study of micro-morphology, we found that the PSS surface has a periodic arrangement of cone-shaped micro-structures, which increases its contact area with PiF by about 56% compared to FSS. Subsequently, the reflection and transmission of FSS and PSS were studied, and the ability of PSS to adjust the blue laser beam was verified. By adjusting the direction of the laser irradiation, the PiF-FSS and PiF-PSS showed distinct differences in their luminescence performance. With the increase of laser power density, the saturation threshold of PSS-PiF was nearly doubled as compared to FSS-PiF, and achieved higher efficiency and better uniformity of warm white light emission. Finally, detailed analyses were conducted on the thermal properties of PiF-FSS and PiF-PSS to elucidate the "thermal limitation" mechanism of PiF under high-power laser irradiation.

2. Experimental section

2.1. Materials

The raw materials used in this experiment are SiO_2 (99%, Aladding), H_3BO_3 (99.9%, Macklin), ZnO (99.9%, Aladding), Na_2CO_3 (99.9%, Macklin), CaO (98%, Macklin), terpineol (95%, Aladding), ethyl cellulose (CP, Aladding), and $Y_3Al_5O_{12}:Ce^{3+}$ (YAG:Ce) yellow phosphor (Shenzhen looking long technology Co., LTD), which are all commercially available.

The sapphire substrates (SS) used were flat sapphire substrate (FSS, Shandong Original Crystal Electronic Technology Co., Ltd.) and patterned sapphire substrate (PSS, Shanghai Puruido Material Optical Materials Co., Ltd.), both with dimensions of 20.0 mm × 20.0 mm× 0.5 mm. In addition, the smooth surfaces of both types of SSs were polished uniformly to ensure a similar roughness.

2.2. Preparation of matrix glass powder

Appropriate amounts of raw materials were weighted based on the composition of $30SiO_2$-$22B_2O_3$-32ZnO-$10Na_2O$-6CaO (%, in mole). They were well mixed and ground in an agate mortar. Then, the mixtures were melted in an alumina crucible placed in Muffle furnace at 1200 °C for 1 h. The molten glass liquid is water quenched and then thoroughly ground to obtain matrix glass powder which was filtered through a 200 mesh sieve. Moreover, physical/thermal characteristics of the matrix glass are shown in Fig. S1.

2.3. Preparation of YAG:Ce PiF

YAG:Ce PiF was solidified on the surface of a SS through a solid-phase co-sintering process, as shown in Fig. 1. Firstly, glass powder and yellow phosphor powder were weighted in a ratio of 1:5 and mixed in an agate mortar. They were then evenly mixed with an organic vehicle in a ratio of 3:1 to form a slurry, which the organic vehicle consists of 3% (in mass) ethyl cellulose and 97% (in mass) terpineol. Next, the slurry was uniformly coated onto the surface of the SS utilizing a blade. After that, the substrate was heated at 300 °C for 8 h to expel organic solvents, and then sintered at 640 °C for 20 min. Finally, the substrate was gradually cooled down to room temperature to obtain the desired PiF structure. Additionally, for PSS, the surface exhibiting a microstructure was designated as the front (F), while the smooth surface was referred to as the back (B). Similarly, once the film layer was prepared, the surface with the film layer was recognized as the front, and the surface without the film layer was denoted as the back.

2.4. Characterizations

The identification of crystalline phases in the glass powder, YAG:Ce phosphor, and PiF was carried out using a powder X-ray diffractometer (XRD-7000, Shimadzu) equipped with a Cu-K_α irradiation source. The microstructures were analyzed using atomic force microscopy (AFM, Cypher ES, Oxford) and scanning electron microscopy (SEM, SUPRA55 SAPPHIRE, Zeiss) with an energy dispersive spectrometer (EDS) for elemental analysis. Reflectance spectra of FSS, PSS, and PiF were obtained from 300 nm to 800 nm using a UV-Vis spectrophotometer (UV-2550, Shimadzu). Photoluminescence excitation (PLE), photoluminescence (PL) spectra, and fluorescence decay curves were examined using a steady-state and transient fluorescence spectrometer (FLS1000, Edinburgh) with a 450 W Xenon lamp and a 450 nm laser as the excitation

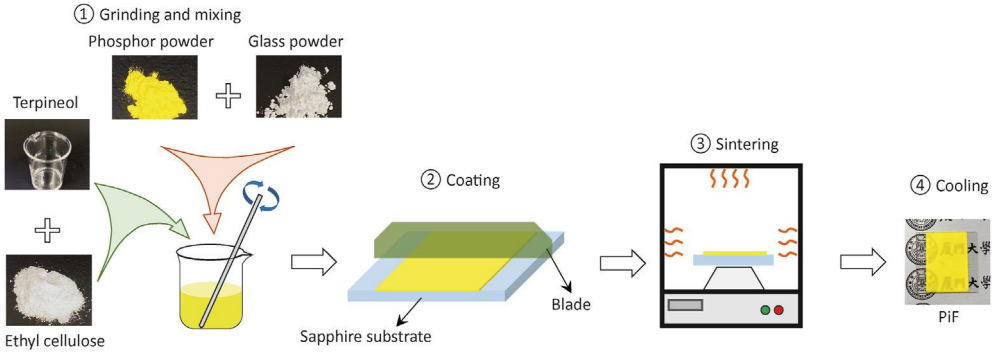

Fig. 1. Schematic of the fabrication process of the PiF.

source. The internal and external quantum efficiency (IQE and EQE) were measured using the FLS1000 instrument with an integrating sphere accessory (N-M01, Edinburgh). Temperature-dependent PL measurements were collected using a modular fluorescence spectrometer (SpectraPro-2300i, Acton). Luminous flux (LF), luminous efficiency (LE), correlated color temperature (CCT), color rendering index (CRI), and electroluminescent (EL) spectra were recorded using a 30 cm diameter integrating sphere connected to a photodetector (HAAS-2000, Everfine). Thermal conductivity and thermal diffusivity were measured using a flash conductometer (LFA467, Netzsch). The surface temperature of the PiF under laser irradiation was measured using an infrared thermal imaging camera (Ti10, Fluke). The optical power of the 450 nm LD (5 W, Nichia) with a fixed spot size (0.547 mm^2) was measured using a laser power meter (PD300, Ophir).

3. Results and discussion

3.1. Structure and luminous properties of YAG:Ce PiF

The SEM images shown in Fig. 2a and b are taken from glass powder and YAG:Ce phosphor powder, respectively. It can be observed that the glass powder exhibits poor particle uniformity, with significant amounts of small particles ranging from 2 μm to 5 μm, in addition to larger particles of approximately 50 μm. In contrast, the particle size distribution of YAG:Ce phosphor is relatively uniform. The SEM image of the YAG:Ce PiF surface is shown in Fig. 2c, where transparent phosphor particles can be observed forming a dense network adhering to the molten and shrunk glass. However, there are many pores, and a denser layered structure cannot be formed. The EDS spectrum of the sample in Fig. 2d confirms that the shape of the glass and phosphor powder is fully consistent with the observed results. Subsequently, the XRD pattern in Fig. 2e shows that the PiF is mainly composed of amorphous glass and garnet phase, with no impurity phase, which further indicates that there was no corrosion reaction between the substrate glass and YAG:Ce crystal during the high-temperature sintering process.

Fig. 3a shows the PLE and PL spectra of YAG:Ce phosphor and PiF. All excitation spectra are composed of two absorption peaks at 340 nm and 460 nm, corresponding to the excitation transitions of Ce^{3+} from the $4f \rightarrow 5d_2$ and $4f \rightarrow 5d_1$ energy levels. Under excitation at 460 nm, the PL spectrum exhibits a broad asymmetric band, which can be attributed to the typical transition of Ce^{3+} from the $5d_1$ excited state to the $2F_{7/2}$ and $2F_{5/2}$ ground state configurations. Fig. 3b displays the fluorescence decay curves of YAG:Ce phosphor and PiF, which can be fitted by a single exponential formula as following Eq. (1) [26]:

$$I(t) = y_0 + A\exp\left(-\frac{t}{\tau}\right) \quad (1)$$

where $I(t)$ represents the fluorescence intensity of the sample at time t, y_0 and A are constants, and τ is the fitted lifetime. The calculated fluorescence lifetimes of Ce^{3+} in YAG:Ce phosphor and PiF are 61.19 ns and 59.56 ns, respectively. The approximate similarity of the fluorescence lifetimes indicates almost no change in the coordination environment of Ce^{3+} as a luminescent center. These luminescent characteristics are similar to those of the original phosphor, confirming the negligible negative impact of thermal corrosion during the co-sintering process. Similarly, the results of IQE in Fig. 3c further demonstrate that the YAG:Ce crystals retain nearly all the performance of the original phosphor, but the EQE of PiF is significantly reduced due to absorption and scattering by the glass and pores [11,27]. The integral intensities corresponding to the temperature-dependent PL spectra of YAG:Ce phosphor and PiF (see Fig. S2) were depicted in Fig. 3d. Obviously, PiF withstands heat much better than phosphor. The prepared YAG:Ce PiF exhibits excellent performance, meeting the basic requirements of high-power laser-driven phosphor conversion materials.

3.2. Micromorphology of FSS, PSS and PiF

Fig. 4a and b shows the AFM images of FSS and PSS. The surface roughness of FSS is 0.31 nm, and compared to phosphor glass film, its surface is extremely smooth. On the other hand, the surface of PSS is featured with regular convex structures, with a corresponding surface roughness of 118.8 nm. It can clearly distinguish between the different surface morphologies of the two substrates. Fig. 4c and d shows SEM images that give a more detailed view of PSS. The surface microstructure of PSS is a clear cone shape arranged in a periodic pattern with a period length of 3.14 μm. The corresponding circular bottom diameter of the monomer is approximately 2.71 μm, and the height is approximately 1.62 μm. Subsequently, the cross-sectional morphologies of the PiF prepared on different substrates were analyzed. Fig. 4e shows a SEM image of the sample based on FSS. Due to the high proportion of phosphor powder in the PiF, the melting of the glass during sintering does not completely fill the gaps between the particles. In addition to the remaining pores on the surface (see Fig. 2c), pores of various sizes can be observed at the interface between the film layer and the SS. In Fig. 4f, the enlarged image shows that the glass powder shrinks and deforms after melting, adhering to the adjacent phosphor powder particles and smooth substrate to complete the solidification of PiF. Meanwhile, the cross-sectional morphology of the PSS-based PiF is shown in Fig. 4g and h, which is consistent with the above analysis. The main difference is related to the interface

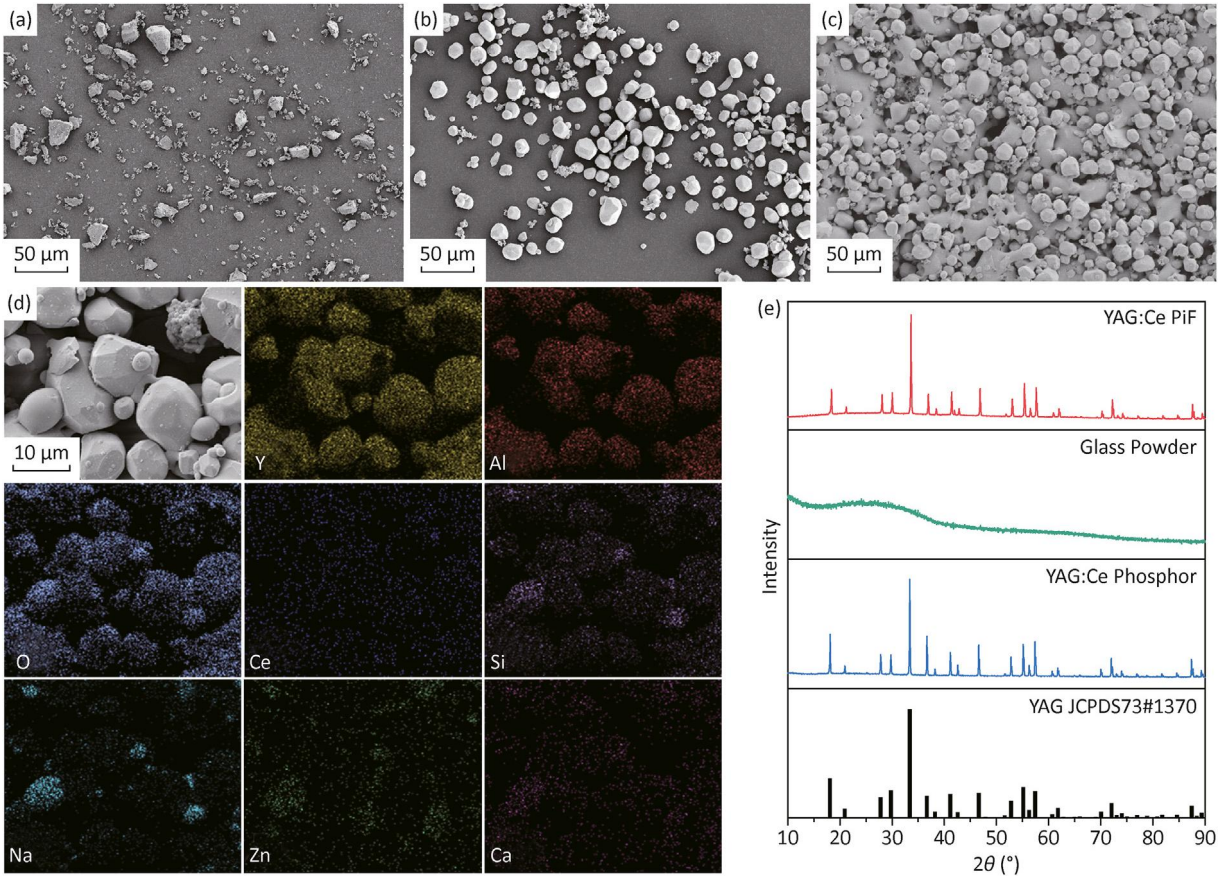

Fig. 2. SEM images of the (a) glass powders, (b) YAG:Ce phosphor, (c) PiF; (d) EDS spectra of the PiF; (e) XRD patterns of the samples.

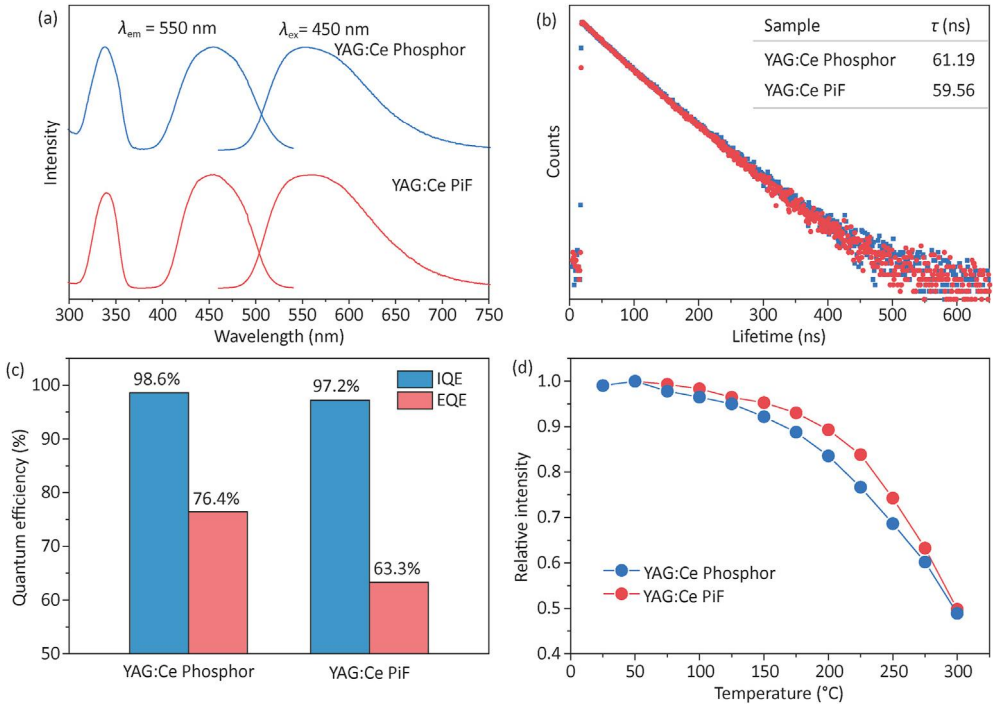

Fig. 3. (a) PLE and PL spectra, (b) fluorescence decay curves, (c) IQE and EQE, (d) Temperature-dependent relative emission intensity of the YAG:Ce phosphor and PiF.

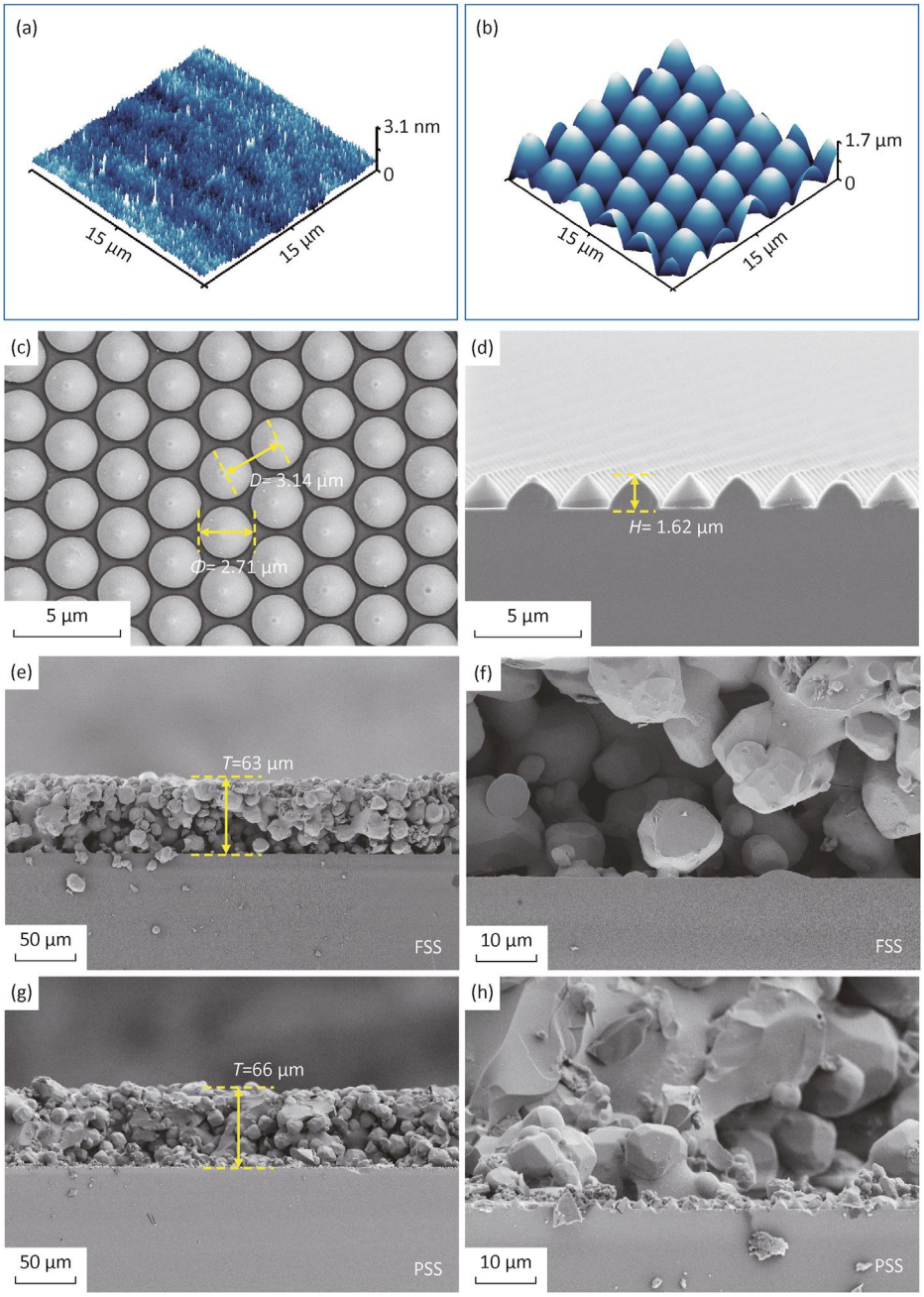

Fig. 4. AFM images of the (a) FSS and (b) PSS; SEM images on the (c) surface and (d) cross-section of the PSS; Cross-section SEM images of the (e–f) PiF-FSS and (g–h) PiF-PSS.

between the film layer and the PSS. Thanks to the use of fine glass powder, it is easier to embed the surface of PSS during the coating phase, and once the glass is melted, it can easily fill the gaps in the microstructure, resulting in a stronger bond. According to the calculation formula for the approximate cone, the presence of the microstructure increases the surface area by approximately 56% compared to the original flat surface, which further strengthens the contact between PiF and PSS. It is worth noting that the thickness of the PiF on both substrates is controlled at around 60 μm. This thickness has already been confirmed as the preferred thickness in the literature [8].

3.3. Optical properties of FSS and PSS under laser irradiation

Fig. 5a shows the photos of the FSS and PSS. It can be seen that the PSS has distinct visual characteristics and presents noticeable color patterns under natural light. However, it also has a high visible light transmittance similar to FSS, which clearly meets the basic requirement of serving as a PiF transparent substrate. After the uniform polishing treatment on both surfaces of FSS and a single surface of PSS, the reflection spectra of the two substrates were tested, including the patterned surface of PSS, as shown in Fig. 5b. Obviously, smooth planes will cause specular reflection,

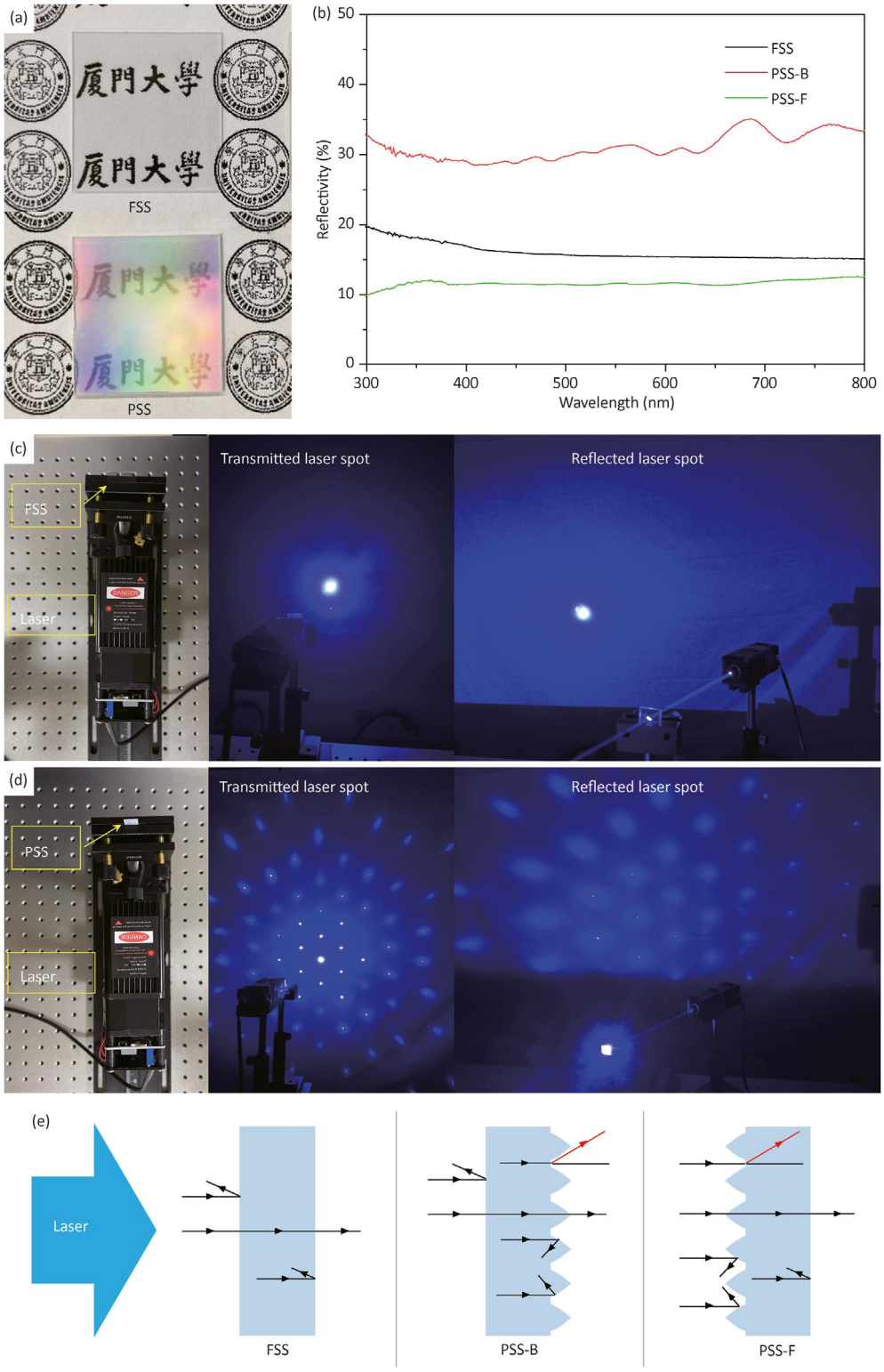

Fig. 5. (a) Photographs and (b) reflectance spectra of the FSS and PSS; Images of transmitted and reflected spots of the (c) FSS and (d) PSS under blue laser irradiation; (e) Schematic diagram of light from the FSS, PSS-B and PSS-F under laser irradiation.

resulting in a reflectivity of 15%–20% for FSS. Regarding the difference between the smooth surface (PSS-B) and the patterned surface (PSS-F) of the PSS, there is a significant difference in their respective reflectance. The reflection of smooth and patterned surfaces ranges from 30% to 40% and 10%–13%, respectively. This means that the surface microstructure of PSS selectively reduces the reflection and anti-reflection in the direction of incident light, that is, it can effectively reduce the reflection from the front surface and intensify the reflection from the back surface. Considering the optimal excitation wavelength of PiF (see Fig. 3a), we fixed the light

source on a single blue laser and tested the optical performance of FSS and PSS under actual conditions. The corresponding spot photos of transmission and reflection are shown in Fig. 5c and d. Due to the high transmittance at the visible band, the laser spot does not show obvious deformation or divergence after transmission through the FSS, and still maintains the aggregated point-like spot. The same is true for the reflection spot results. However, when the same blue laser is irradiated on the PSS, the transmitted light spot presents a centrally symmetrical and evenly dispersed point pattern. The intensity of the light spot in the center is the highest, while the peripheral bright spots surround the center and decrease in intensity as the distance increases. The reflected light spot shows the same result. It is worth noting that regardless of whether the incident laser is from the front or the back of the PSS, the transmitted and reflected light spots show a scattered spot distribution and only change in intensity. To analyze the optical differences between FSS and PSS under laser irradiation, a light schematic diagram was constructed as shown in Fig. 5e. Due to the smooth plane of FSS, when the incident laser penetrates vertically, only specular reflection occurs on the plane, so the light spot does not change. When the incident laser hits the optical surface of the PSS (PSS-B), specular reflection occurs first. The transmitted laser reaches the interface between the pattern surface and the air and is deflected due to the influence of the tapered microstructure. According to the measurement data in Fig. 4c, the spacing between microstructures is 0.43 μm, which is very close to the wavelength, 450 nm, of the incident laser. Therefore, strong diffraction occurs when light passes through the interface and the deflected light aggregates. At the same time, because the microstructure itself is also transparent, the highly polymerized laser beam still maintains vertical penetration, resulting in a much lower intensity of peripheral light spots after diffraction than the center [23]. In addition, when light passes through the PSS, internal reflection still occurs near the interface, including the inner curved surface of the microstructure, so that the reflected light spots also show the same point-like distribution. However, under the influence of reflection, the intensity of the reflected light spot is low. Based on the above results, we believe that the PSS has a better astigmatism effect than the FSS, which plays a key role in the overall luminous performance after composite PiF, and is conducive to enhancing luminous performance and homogenizing white light.

3.4. Luminescence properties of PiF-FSS and PiF-PSS under laser irradiation

Fig. 6a shows the reflectance spectra and photographs of PiF-FSS and PiF-PSS, including the reflection parameters of the back and front surfaces of individual samples. Due to the consistency of the PiF layer, the appearance variation between PiF-FSS and PiF-PSS is not particularly evident. However, the reflectivity of the samples in the visible light region is relatively higher than that of the single substrate, with PiF-PSS-B exhibiting the highest reflectivity. This is consistent with the results in Fig. 5b, which is mainly due to the increase in interfacial reflection caused by the microstructure on the surface of PSS together with the fused glass, which amplifies the reflected light from the back side. In addition, both PiF-FSS and PiF-PSS exhibit noticeable absorption or transmission at 450 nm. Therefore, an illumination device was specifically constructed as shown in Fig. 6b to verify the actual luminescence performance of the samples. A 450 nm laser was employed as the excitation light source, and the samples were positioned in a reflective cup for optimal light collection and mixing. Finally, the light was projected onto a screen through an outlet, and the spot pattern image was obtained as shown in Fig. 6c. Firstly, the laser uniformly illuminates the back surface of the samples. The spot corresponding to PiF-FSS-B appears white, with a clustered blue laser spot in the center and weak blue light in other positions. This is due to the reflection of the substrate surface on the laser and the insufficient absorption of the laser by the film layer, which results in a significant portion of blue light passing through the sample. The same situation also occurs in PiF-PSS-B, and due to the high interface reflection, more blue light that is not absorbed by the PiF layer is scattered, resulting in clustered blue areas at the edges and center of the spot. Simultaneously, a scattered spot distribution of the blue light spots, as shown in Fig. 5d, was observed. Subsequently, when the laser hits the front surface of the samples, the spot change is obvious for PiF-FSS and PiF-PSS well. The spot of PiF-FSS-F appears mainly bright yellow, with a blue laser spot still present in the center, but reduced in intensity, and no other scattered blue light aggregation areas are observed. As shown in Fig. 6d, the luminance uniformity of the PiF-PSS-F spot is notably superior to that of the PiF-FSS-F spot, with the exceptions of a minor diffusion of blue light in the central area. When the laser is irradiated on the surface of the PiF, the presence of irregular particles and pores on the surface of the film significantly increases its roughness, resulting in effective reduction of reflectivity for blue laser and maximum absorption of blue light [28,29]. Moreover, due to the structure of the interface between the PSS and the PiF, when the light reaches this area, diffraction occurs and causes the light to spread, hence restraining the unabsorbed and still aggregated blue laser beam [30]. In summary, the presence of microstructures scatters the light more, acting as a diffuser and ultimately providing a more uniform mixed light distribution [31].

Next, the luminescence performance of the sample was investigated by changing the incident laser power density, as shown in Fig. 7a–d. The LF of the samples increased linearly with the increase in laser power density. When the laser power density reached 3.29 W/mm^2, PiF-FSS-F first reached 'saturation' and then began to decline. The saturation power density for PiF-PSS-F was 6.29 W/mm^2. PiF-FSS-B exhibited the highest saturation power density at 9.32 W/mm^2, while the saturation threshold for PiF-PSS-B could not be determined due to exceeding the equipment test capability. The corresponding LF peak values were 378.8, 721.2, 897.9 lm and 553.6 lm, respectively. On the other hand, in Fig. 7b, both PiF-FSS-F and PiF-PSS-F exhibited a peak in the LE when the initial laser power density was reached, followed by a slow decline. The average LE for both samples exceeded 220 lm/W, and their variation trends were similar, primarily due to the direct irradiation of the laser on the PiF surface. In contrast, the LE of PiF-FSS-B and PiF-PSS-B exhibited relatively stable fluctuations with increasing laser power density. The average LE for PiF-FSS-B remained at 180 lm/W, while PiF-PSS-B had the lowest average LE, approximately 150 lm/W. Similarly, a turning point in the LE occurred when saturation was reached. Chen *et al.* confirmed that laser incidence on rough surfaces can directly enhance the LE of phosphor materials, which is consistent with the afore-mentioned findings [30]. In Fig. 7c, the average CCT of PiF-FSS-F and PiF-PSS-F is approximately 4500 K, significantly lower than that of PiF-FSS-B (approximately 6600 K) and PiF-PSS-B (the CCT of PiF-PSS-B is higher, exceeding the range of device testing, and is displayed as a fixed value of 25,000 K). The CRI values shown in Fig. 7d exhibit similarities to the results of CCT analysis, but due to the yellow broadband emission limitation of YAG:Ce, the CRI value of the mixed light remained between 62 and 75. The color coordinate variation of the emitted light is shown in Fig. 7e. Apart from PiF-PSS-B, which did not meet the basic requirements for white light illumination, the emission of the other samples presented white light (including warm and cool white light regions), corresponding to the color of the light spot in Fig. 6c. Fig. 7f shows the EL spectra of PiF-FSS and PiF-PSS under the same power density blue light excitation. PiF-FSS-B and PiF-PSS-B exhibited relatively low absorption of the blue laser light,

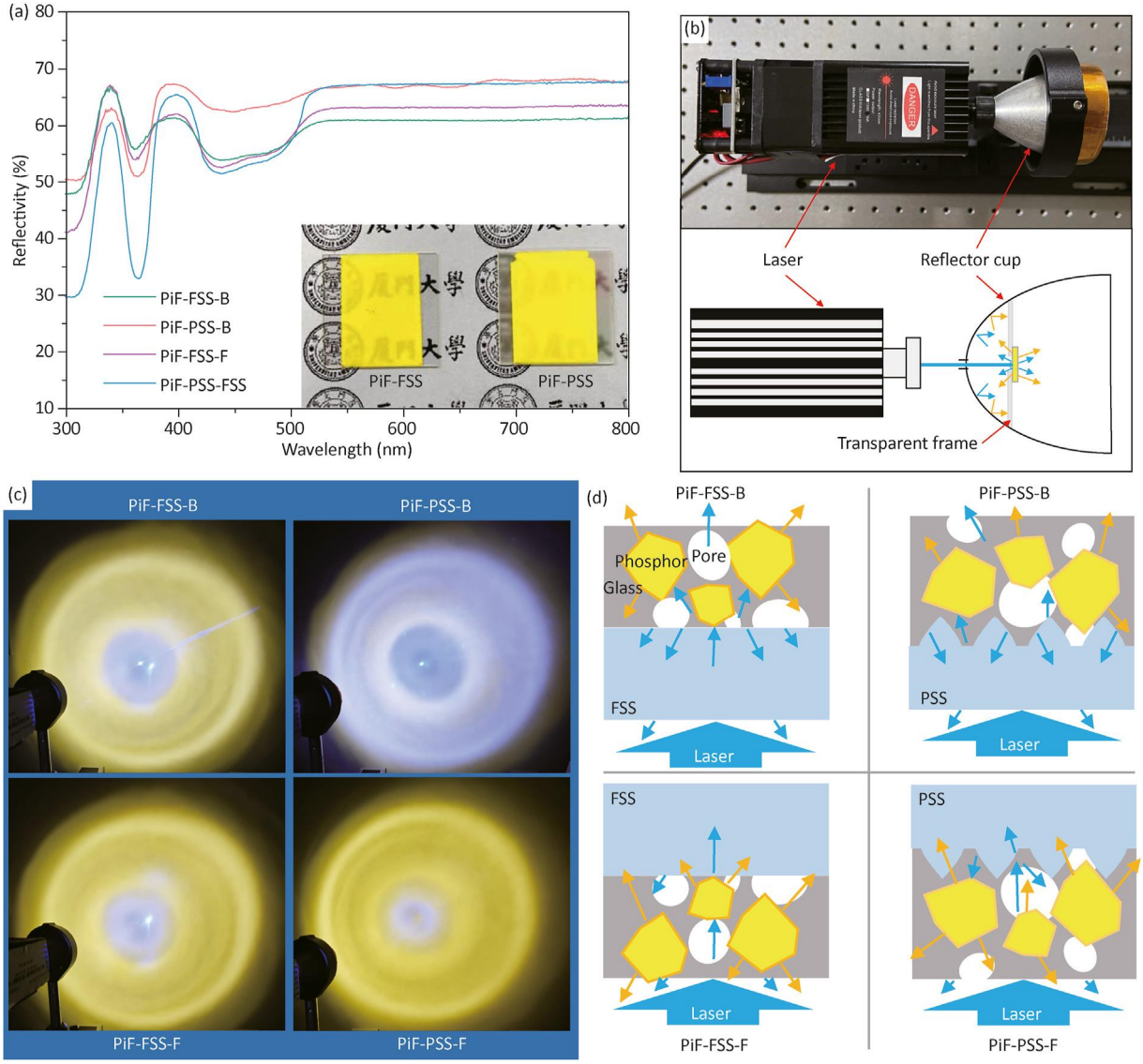

Fig. 6. (a) Reflectance spectra of the PiF-FSS and PiF-PSS, inset shows the photograph; (b) Schematic diagram of the device for blue laser pumping sample to output mixed light; (c) Spot photographs and (d) luminescence schematic of the samples under the same power laser irradiation.

resulting in weaker emission intensity. PiF-PSS-B had the highest reflectance (see Fig. 6a) and the weakest absorption ability for blue light conversion. When the direction of laser irradiation is changed, the difference in absorption and conversion ability of blue laser between PiF-FSS-F and PiF-PSS-F becomes relatively small due to the similar performance of PiF. This ultimately results in a weak performance gain such as LE, CCT and CRI of the PSS on PiF.

However, the laser-driven light source constructed in this study maintains the original levels of LF, LE, and saturation power density even under conditions of low CCT down to 4500 K, and the efficient warm white light is particularly important for the lighting industry. In addition, we believe that this PiF-PSS still has the potential to explore higher luminous performance.

3.5. Thermal properties of PiF-FSS and PiF-PSS under laser irradiation

In fact, under continuous laser irradiation, heat is generated and the luminescence performance of phosphor materials is inevitably affected by the temperature. Fig. 8a shows the thermal conductivity performance of PiF-FSS and PiF-PSS at different temperatures. Under normal conditions, PiF-PSS has the highest thermal expansion coefficient and thermal conductivity, with values of 6.96 mm^2/s and 16.4 W/(m·K), respectively, which are 58% and 30% higher than those of PiF-FSS. As the temperature increases to 300 °C, the difference between the two gradually narrows, but the heat-conducting capabilities of PiF-PSS are always superior to those of PiF-FSS. This is clearly a direct effect of the PSS surface structure combined with PiF, and confirms that increasing the coupling surface has a positive effect on the heat transfer efficiency [32,33]. Fig. 8b shows the temperature variation of the sample under laser irradiation with different power densities. Regardless of whether the laser is incident from the back or front, the surface temperature of PiF-FSS is higher than that of PiF-PSS, and this tend increases with the increase of laser power density. Considering the results of Fig. 6, the main reason for the low surface temperature of PiF-PSS-B is that the blue laser is strongly reflected (*i.e.*, not absorbed and converted by PiF) and thus generates negligible cumulative heat. The temperature difference between PiF-FSS-F and PiF-PSS-F is obviously dependent on the gained effect of PSS structure on

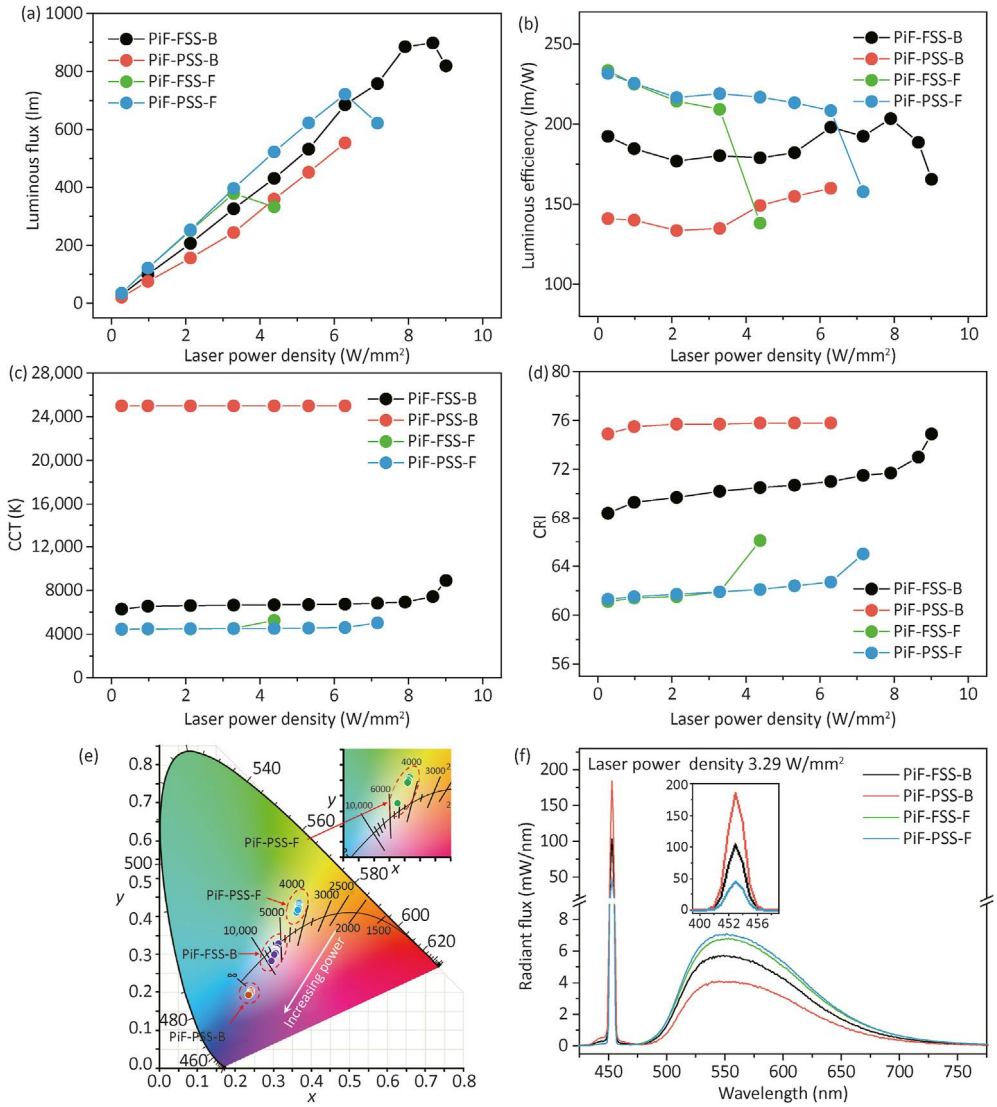

Fig. 7. (a) LF, (b) LE, (c) CCT, (d) CRI and (e) CIE color coordinates of the samples at different laser power densities; (f) EL spectra of the samples at laser power density of 3.29 W/mm^2.

thermal conduction. And this is more intuitive in the thermal imaging data of Fig. 8c. The distribution of surface temperature of PiF-PSS-F is uniform, while the heat of PiF-FSS-F is focused to the luminescence center, resulting in a higher temperature in the center area. Fig. 8d provides an analysis of the internal structure and heat transfer path of PiF. The Ce^{3+} in YAG:Ce phosphor particles functions as a luminescent activator, exhibiting both radiative and non-radiative recombination when excited by blue light. In the nonradiative recombination process, heat is generated and radiated out in the form of phonons, which is rapidly transported along the YAG lattice and forms a heat source [6]. However, during the heat transfer process, phonons are hindered by two media: glass and pores. The thermal conductivity of glass is approximately 1 W/(m·K), while the main component of pores is air, with a thermal conductivity of approximately 0.02 W/(m·K). Due to the random distribution of glass and pores, the transmission path of phonons becomes complex (see Fig. 8d), resulting in an increase in the thermal resistance of the interface and a sudden decrease in the transfer rate [34]. Clearly, the consequence is the rapid accumulation of heat, resulting in regional warming. The Ce^{3+} is affected by high temperatures and undergoes thermal quenching. A coordinate model of a single configuration has been established in Fig. 8e to explain this mechanism [35]. After accumulating enough thermal energy ΔE, the electrons in the $5d_1$ energy level are brought to the intersection point of the $5d_1$ and 4f energy level, satisfying the basic conditions for non-radiative crossing relaxation [36]. After the $5d_1 \rightarrow 4f$ transition occurs, the electrons return to the ground state through vibrational relaxation, similar to the multi-photon non-radiative relaxation that occurs in the 4f–4f transition process [37,38]. In other words, the $5d_1 \rightarrow 4f$ non-radiative crossing relaxation is mainly attributed to the large horizontal shift between the 4f and $5d_1$ parabolas caused by phonon excitation, and this process can be described by the non-radiative transition rate R_{nr} as following Eq. (2) [39,40]:

$$R_{nr} = A_{nr} \times \exp\left(-\frac{\Delta E}{kT}\right) \quad (2)$$

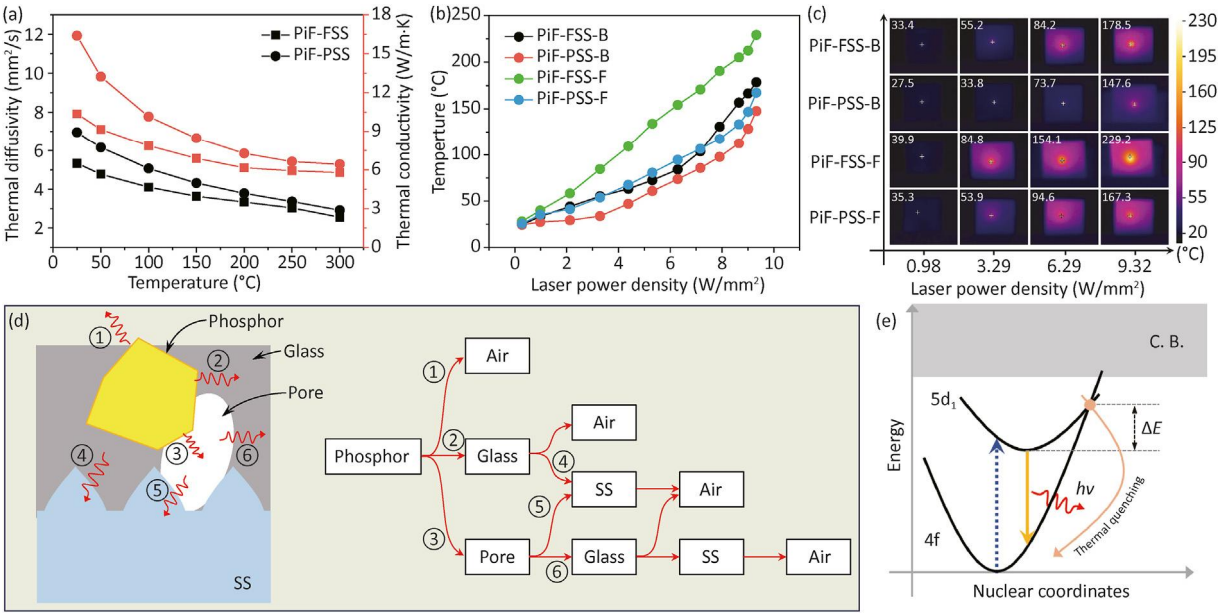

Fig. 8. (a) Thermal diffusivity and thermal conductivity of the samples at different temperatures (25–300 °C); (b) Maximum surface temperature of the samples at different laser power densities; (c) Thermal images of the samples at selected laser power densities (0.98, 3.29, 6.29 W/mm^2 and 9.32 W/mm^2); (d) Internal heat transfer mechanism and path of the PiF; (e) Configurational coordination diagrams illustrating the thermally quenching of Ce^{3+}.

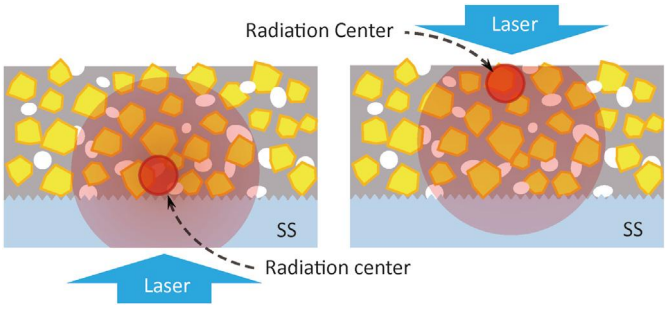

Fig. 9. Schematic diagram of the radiation center position of PiF with respect to the direction of laser irradiation.

where A_{nr} is the attempt rate of non-radiative recombination, k is the Boltzmann constant (1.38×10^{-23} J/K), and T is the temperature. As the temperature increases, the rate of non-radiative transitions significantly increases, and as a result, more active centers are converted from radiative recombination to non-radiative recombination. These "quenching centers" will then spread outwards with the propagation of phonons. Therefore, the PiF region that is first exposed to laser irradiation will experience thermal saturation earlier, and as the laser power increases, the area of quenching will gradually increase, thus limiting the emission intensity.

In addition, due to the significant difference in the thermal conductivity of the SS and PiF, the position of the corresponding radiation center will also change with the change of laser radiation direction, as shown in Fig. 9. When the laser is incident from the backside, the phosphor crystals near the substrate first absorb the blue light and release heat. There are two heat transfer directions along the longitudinal axis: one is directed towards the interior of the PiF, and the other is towards the substrate. Substrate with higher thermal conductivity exhibits a more rapid dissipation of heat compared to the PiF, enabling them to endure higher power density laser irradiation (see Fig. 7a). However, when the laser is incident from the front, the phosphor crystals near the PiF surface absorb the blue light and release heat, but much of the heat propagates inside the PiF instead of being dissipated into the air environment. The slower internal heat transfer rate of the PiF then leads to a rapid temperature rise, resulting in the earlier saturation threshold shown in Fig. 7a. In summary, the luminescence performance of PiF-FSS and PiF-PSS is significantly affected by the direction of laser irradiation, especially the high heat-conducting capability of PiF-PSS is fully utilized when the laser is irradiated from the front. However, due to the limitations of the PiF structure, the saturation threshold did not exceed the highest value of PiF-FSS, which is worth investigating and improving in future research.

4. Conclusions

In this work, PiF was prepared by sintering silicate glass with YAG:Ce phosphor on the surface of FSS and PSS using low-temperature co-sintering technology. YAG: Ce PiF is less affected by high temperature and glass corrosion, and still has good luminous characteristics. Microscopic observations revealed that the PSS possessed periodic arrays of cone-shaped structures, which increased the surface area by approximately 56%, and strengthened the adhesion between the PiF and the substrate, in contrast to the planar surface of FSS. Reflectance spectra showed that the FSS exhibited about 15% specular reflection, whereas the PSS exhibited enhanced and decreased reflection on the back and front surfaces, respectively. Thanks to its surface microstructure, the PSS exhibited strong modulation to the blue laser compared to FSS, and showed scattered light spots due to diffraction. Similarly, after consolidating PiF, the spot image confirmed the positive effect of PSS on the improvement of the optical uniformity. With the change in laser power density, PiF-PSS-F achieved not only higher LE (over 220 lm/W) and lower CCT (approximately 4500 K), but also an increased

saturation power density of up to 91% compared to PiF-FSS, reaching 6.29 W/mm^2. This is obviously influenced by the higher heat-conducting capabilities of PiF-PSS than PiF-FSS, and thus reveals the thermal quenching mechanism of PiF. These results complement and enhance the understanding of the impact of interface structure between SSs and PiG on their luminescence properties.

Declaration of competing interest

The authors declare that they have no known competing financial interests or personal relationships that could have appeared to influence the work reported in this paper.

CRediT authorship contribution statement

Wenting Ding: Conceptualization, Data curation, Formal analysis, Investigation, Methodology, Validation, Visualization, Writing – original draft. **Shuai Yang:** Methodology, Project administration. **Xin Hou:** Methodology, Project administration. **Tao Yang:** Formal analysis. **Rongbin Xu:** Project administration, Resources, Writing – review & editing. **Yang Mei:** Project administration, Resources. **Leiying Ying:** Methodology, Project administration, Validation. **Miao Lu:** Resources. **Baoping Zhang:** Funding acquisition, Methodology, Project administration, Resources, Supervision, Writing – review & editing.

Acknowledgements

This work was supported by the National Natural Science Foundation of China (Nos. U21A20493, 62234011 and 62104204) and the President's Foundation of Xiamen University (No. 20720220108).

Appendix A. Supplementary data

Supplementary data to this article can be found online at https://doi.org/10.1016/j.jmat.2024.04.014.

References

[1] Wang L, Yang H, Zhang Y, Liang Y, Zhang J, Mei E, et al. All-inorganic high efficiency LuAG:Ce^{3+} converter based on phosphor-in-glass for laser diode lighting. J Alloys Compd 2022;892:161882.
[2] Xu J, Yang Y, Guo Z, Corell DD, Du B, Liu B, et al. Comparative study of Al_2O_3-YAG:Ce composite ceramic and single crystal YAG:Ce phosphors for high-power laser lighting. Ceram Int 2020;46(11):17923–8.
[3] Wang P, Lin H, Lin S, Sui P, Xu J, Cheng Y, et al. Reducing the cyan-cavity: $Lu_2MAl_4SiO_{12}$:Ce^{3+} (M = Mg, Ca, Sr and Ba) phosphor-in-glass film towards full-spectrum laser-driven lighting. J Mater Chem C 2022;10(43):16337–46.
[4] Deng T, Huang L, Li S, Zhu Q, Wang L, Takeda T, et al. Thermally robust orange-red-emitting color converters for laser-driven warm white light with high overall optical properties. Laser Photon Rev 2022;16(6):2100722.
[5] Xu L, Wang X, Wang L, Bao S, Wang Y, Liang X, et al. Design of a novel $La_3Si_6N_{11}$:Ce^{3+} phosphor-in-glass film for high power laser lighting: luminous efficiency toward 200 lm·W^{-1}. ACS Sustainable Chem Eng 2022;10(38):12817–25.
[6] Lin S, Lin H, Huang Q, Yang H, Wang B, Wang P, et al. Highly crystalline $Y_3Al_5O_{12}$:Ce^{3+}phosphor-in-glass film: a new composite color converter for next-generation high-brightness laser-driven lightings. Laser Photon Rev 2022;16(12):2200523.
[7] Wang Z, Huang F, Cai M, Zhang X, Deng D, Xu S. Novel ultra-wideband fluorescence material: defect state control based on nickel-doped semiconductor QDs embedded in inorganic glasses. J Materiomics 2023;9(2):338–44.
[8] Huang Q, Sui P, Huang F, Lin H, Wang B, Lin S, et al. Toward high-quality laser-driven lightings: chromaticity-tunable phosphor-in-glass film with "phosphor pattern" design. Laser Photon Rev 2022;16(7):2200040.
[9] Xu J, Wang L, Gu W, Jiang Z, Chen X, Hu B, et al. Emitting area limitation *via* scattering control in phosphor film realizing high-luminance laser lighting. J Eur Ceram Soc 2022;42(2):608–15.
[10] Wen Q, Wang Y, Zhao C, Xu L, Wang X, Xu Y, et al. Ultrahigh power density LuAG:Ce green converters for high-luminance laser-driven solid state lighting. Laser Photon Rev 2023;17(6):2200909.
[11] Zhang X, Yu J, Wang J, Lei B, Liu Y, Cho Y, et al. All-Inorganic light convertor based on phosphor-in-glass engineering for next-generation modular high-brightness white LEDs/LDs. ACS Photonics 2017;4(4):986–95.
[12] Wang H, Mou Y, Peng Y, Zhang Y, Wang A, Xu L, et al. Fabrication of phosphor glass film on aluminum plate by using lead-free tellurite glass for laser-driven white lighting. J Alloys Compd 2020:814152321–7.
[13] Wang L, Liu J, Xu L, Bao S, Wang Y, Zhang J, et al. Realizing high-power laser lighting: artfully importing micrometer BN into Ce: GdYAG phosphor-in-glass film. Laser Photon Rev 2022;17(2):1–9.
[14] Peng Y, Yu Z, Zhao J, Wang Q, Liu J, Sun B, et al. Unique sandwich design of high-efficiency heat-conducting phosphor-in-glass film for high-quality laser-driven white lighting. J Adv Ceram 2022;11(12):1889–900.
[15] Chung WJ, Nam YH. Review—a review on phosphor in glass as a high power LED color converter. ECS J Solid State Sci Technol 2019;9(1):016010.
[16] Yue X, Xu J, Lin H, Lin S, Li R, Wang B, et al. β-SiAlON:Eu^{2+} phosphor-in-glass film: an efficient laser-driven color converter for high-brightness wide-color-gamut projection displays. Laser Photon Rev 2021;15(11):2100317.
[17] Yang H, Zhang Y, Zhang Y, Zhao Y, Liang X, Chen G, et al. Designed glass frames full color in white light-emitting diodes and laser diodes lighting. Chem Eng J 2021:414128754.
[18] Wu H, Hao Z, Pan G, Zhang L, Wu H, Zhang X, et al. Phosphor-SiO_2 composite films suitable for white laser lighting with excellent color rendering. J Eur Ceram Soc 2020;40(6):2439–44.
[19] Bao S, Liang Y, Wang L, Wang L, Xu L, Wang Y, et al. Superhigh-luminance Ce:YAG phosphor in glass and phosphor-in-glass film for laser lighting. ACS Sustainable Chem Eng 2022;10(24):8105–14.
[20] Zheng P, Li S, Wang L, Zhou T-L, You S, Takeda T, et al. Unique color converter architecture enabling phosphor-in-glass (PiG) films suitable for high-power and high-luminance laser-driven white lighting. ACS Appl Mater Interfaces 2018;10(17):14930–40.
[21] Wei C, Cao D, Dong Y, Xiong J, Trofimov Y, Lishik S, et al. Enhancing luminous flux and color rendering of laser-excited YAG:Ce^{3+} single crystal phosphor plate via surface roughening and low-temperature sintering a $CaAlSiN_3$:Eu^{2+} phosphor-in-borate glass. J Lumin 2022:251119225.
[22] Zhang S, Liang M, Yan Y, Huang J, Li Y, Feng T, et al. High luminous efficacy phosphor-converted mass-produced white LEDs achieved by AlN prebuffer and transitional-refraction-index patterned sapphire substrate. Nanomaterials 2022;12(10):1638.
[23] Chou CY, Lai WH, Li XF, Cheng C, Huang CK, Liu CY. Morphological effect of patterned sapphire substrate on efficiency of white-light phosphor LED package. Opt Mater 2021:119111297.
[24] Yang S, Xu H, Long H, Ying L, Luo R, Zhong M, et al. GaN-based green resonant-cavity light-emitting diodes with Al mirror and copper plate. Opt Lett 2022;47(11):2858–61.
[25] Qi Y, Liu Y, Lin C, Deng Y, Bai P, Gao Y, et al. Anisotropic emission of orientation-controlled mixed-dimensional perovskites for light-emitting devices. J Materiomics 2023;9(4):762–7.
[26] Gao G, Li Q, Hao P, Huang X, Luo H. Luminescent properties of $Mg_{1.99}SnO_4$:0.01Mn^{2+} phosphors doped with Zn^{2+}. J Materiomics 2023;9(3):510–5.
[27] Zhu Q, Wang X, Wang L, Hirosaki N, Nishimura T, Tian Z, et al. β-Sialon:Eu phosphor-in-glass: a robust green color converter for high power blue laser lighting. J Mater Chem C 2015;3(41):10761–6.
[28] Zhang L, Sun B, Gu L, Bu W, Fu X, Sun R, et al. Enhanced light extraction of single-surface textured YAG:Ce transparent ceramics for high power white LEDs. Appl Surf Sci 2018:455425–32.
[29] Yang C, Zhang X, Kang J, Wei C, Sang P, Lin S, et al. Recent progress on garnet phosphor ceramics for high power solid-state lighting. J Mater Sci Technol 2023;166:1–20.
[30] Sun B, Zhang L, Huang G, Zhou T, Shao C, Wang K, et al. Surface texture induced light extraction of novel Ce:YAG ceramic tubes for outdoor lighting. J Mater Sci 2018;54(1):159–71.
[31] Huang K, Lai TH, Chen CY. Improved CCT uniformity of white LED using remote phosphor with patterned sapphire substrate. Appl Opt 2013;52(30):7376–81.
[32] Lin T, Chen H, Li S, Wang L, Huang F, Xie R. Bi-color phosphor-in-glass films achieve superior color quality laser-driven stage spotlights. Chem Eng J 2022:444136591.
[33] Wu H, Xu S, Feng L, Mao W, Tao H, Gao Y, et al. Patterned sapphire substrates cause a wavelength shift of green InGaN light-emitting diodes. Opt Mater Express 2020;10(9):2045–53.
[34] Lee D, Kim S, Kim H, Lee S-K. Highly efficient and highly conductive phosphor-in-glass materials for use in LD-driven white-light lamp. Int J Pr Eng Man-GT 2019;6(2):293–303.
[35] Fang H, Zhou B, Wang J, Hu X, Pan Z, Fan S, et al. Y_2O_3-YAG:Ce composite

phosphor ceramics with enhanced light extraction efficiency for solid-state laser lighting. J Mater Chem C 2022;10(42):16147–56.
[36] Ronda CR. Luminescence: from theory to applications. New York: John Wiley & Sons; 2008.
[37] Ma Y, Zhang L, Zhou T, Sun B, Yao Q, Gao P, et al. Weak thermal quenching and tunable luminescence in Ce:$Y_3(Al,Sc)_5O_{12}$ transparent ceramics for high power white LEDs/LDs. Chem Eng J 2020:398125486.
[38] Witkowski D, Rothamer DA. Emission properties and temperature quenching mechanisms of rare-earth elements doped in garnet hosts. J Lumin 2017: 1921250–63.
[39] Di Bartolo B. Advances in nonradiative processes in solids. New York: Springer Science & Business Media; 1991.
[40] Lin Y, Bettinelli M, Karlsson M. Unraveling the mechanisms of thermal quenching of luminescence in Ce^{3+}-doped garnet phosphors. Chem Mater 2019;31(11):3851–62.

Wenting Ding received his B.S. degree from Bengbu University in 2017, and received M.S. degree from Guilin university of technology in 2020. He is currently a Ph.D. candidate in Prof. Baoping Zhang's group in Xiamen University. His research interests focus on luminescent glass material for laser lighting.

Baoping Zhang received his B.S. degree from Lanzhou University in 1983, received Ph.D. degree from University of Tokyo in 1994. He is a full professor at School of Electronic Science and Engineering, Xiamen University. His research focuses on the wide bandgap semiconductor materials and optoelectronic devices, as well as fabrication and application of micro and nano structures.

Rongbin Xu received the B.S. degree from Fuzhou University in 2015, received Ph.D. degree from Xiamen University in 2021. He is currently an Assistant Professor with Xiamen University. His current research focuses on semiconductor devices for optoelectronic applications and MEMS.